Shiwei Zhao
School of Aeronautic Science and Engineering,
Beihang University,
Beijing 100191, China;
Departments of Mechanical Engineering, Civil and Environmental Engineering, Materials Science and Engineering,
Center for Bio-Integrated Electronics,
Northwestern University,
Evanston, IL 60208
e-mail: shiweizhao@buaa.edu.cn

Feng Zhu
School of Logistics Engineering,
Wuhan University of Technology,
Wuhan 430063, China;
Departments of Mechanical Engineering, Civil and Environmental Engineering, Materials Science and Engineering,
Center for Bio-Integrated Electronics,
Northwestern University,
Evanston, IL 60208
e-mail: zhufeng@whut.edu.cn

Zhengang Yan
School of Science,
Harbin Institute of Technology,
Shenzhen 518055, China;
Departments of Mechanical Engineering, Civil and Environmental Engineering, Materials Science and Engineering,
Center for Bio-Integrated Electronics,
Northwestern University,
Evanston, IL 60208
e-mail: yanzhengang@stu.hit.edu.cn

Daochun Li
School of Aeronautic Science and Engineering,
Beihang University,
Beijing 100191, China
e-mail: lidc@buaa.edu.cn

Jinwu Xiang
School of Aeronautic Science and Engineering,
Beihang University,
Beijing 100191, China
e-mail: xiangjw@buaa.edu.cn

Yonggang Huang
Departments of Mechanical Engineering, Civil and Environmental Engineering, Materials Science and Engineering,
Center for Bio-Integrated Electronics,
Northwestern University,
Evanston, IL 60208
e-mail: y-huang@northwestern.edu

Haiwen Luan[1]
Departments of Mechanical Engineering, Civil and Environmental Engineering, Materials Science and Engineering,
Center for Bio-Integrated Electronics,
Northwestern University,
Evanston, IL 60208
e-mail: haiwenluan@u.northwestern.edu

A Nonlinear Mechanics Model of Zigzag Cellular Substrates for Stretchable Electronics

The use of cellular elastomer substrates not only reduces its restriction on natural diffusion or convection of biofluids in the realm of stretchable electronics but also enhances the stretchability of the electronic systems. An analytical model of "zigzag" cellular substrates under finite deformation is established and validated in this paper. The deformed shape, nonlinear stress–strain curve, and Poisson's ratio–strain curve of the cellular elastomer substrate calculated using the reported analytical model agree well with those from finite element analysis (FEA). Results show that lower restriction on the natural motion of human skin could be achieved by the proposed zigzag cellular substrates compared with the previously reported hexagonal cellular substrates, manifesting another leap toward mechanically "invisible" wearable, stretchable electronic systems.
[DOI: 10.1115/1.4046662]

Keywords: stretchable electronics, cellular materials, stress–strain curve, finite deformation, elasticity

1 Introduction

Significant progress has been achieved in materials [1–3] and mechanics [4–16] in offering the capability for stretchable electronics to be deformed into complex shapes without failure in functionality

[1]Corresponding author.
Contributed by the Applied Mechanics Division of ASME for publication in the Journal of Applied Mechanics. Manuscript received February 14, 2020; final manuscript received March 10, 2020; published online March 13, 2020. Assoc. Editor: Pradeep Sharma.

or structure. A recent direction of devising mechanically "invisible" skin-mounted stretchable electronics [17–19], which are ultrasoft and hardly detectable by skin through tactile sensation, demands a new class of compliant elastomer substrates. Like many biological materials, e.g., skin [20,21] and viscid spider silk [22,23], which show "J-shaped" stress–strain behaviors as a result of collagen microstructures, cellular elastomer substrates offer similar behavior [24,25]. The integration of stretchable electronics onto cellular substrates could achieve a similar "J-shaped" stress–strain response as in the biological materials, with a compliant mechanical behavior at low stretching strains and an increasingly stiff response at larger stretching strains to balance wear comfort and structural integrity, shows promising application potential in bio-integrated electronic microsystems and tissue engineering [26–31].

Apart from "J-shaped" stress–strain behavior and high permeability of biofluids [25,32], cellular substrates could achieve much larger stretchability compared with counterpart uniform solid substrates [33]. Some analytical models have been established to investigate the equilibrium and deformation compatibility of hexagonal cellular substrates under finite stretching [34–37]. The stretching behaviors of substrates affect the interfacial shear stress between substrate and human skin, which is one of the key considerations when improving the wear comfort of stretchable, epidermal electronics. The shear stress between hexagonal cellular substrates and human skin is usually higher than the skin sensitivity threshold under finite deformation [37]. In this paper, "zigzag" cellular substrates are investigated and engineered to achieve higher compliance than the previously reported hexagonal cellular substrates, inducing lower interfacial shear stress under finite deformation.

An analytical model to investigate the zigzag cellular substrates with finite deformation is presented in this paper. Results show that the stress–strain relationship calculated by the analytical model matches that from finite element analysis (FEA). The interfacial shear stress between zigzag cellular substrates and human skin is well below the skin sensitivity threshold (20 kPa) [38] in any stretching direction and is noticeably lower than that for the hexagonal cellular substrates [34,35].

2 Analytical Model

The walls of zigzag cellular substrate shown in Fig. 1(*a*) can be modeled as beams when the length of cellular beam segment l is much larger than its width δ. All beam segments in the zigzag substrate are assumed to have the same length l in this study. The thickness of zigzag cellular substrates is assumed to be larger than the width of walls. For uniaxial stretching along x-/y-axis, the basic unit is denoted in the dashed rectangle in Fig. 1(*a*). 1/8 of the basic unit is chosen for analysis on account of symmetry as presented in Fig. 1(*b*). A local coordinate system $\{\bar{x}_i, \bar{y}_i\}$ is constructed as shown in Fig. 1(*b*). The $\bar{x}_i$-axis is parallel to the beams of zigzag cellular substrate, which is also illustrated in Fig. 2. The stretching force per unit thickness acting on the 1/8 basic unit can be denoted as P. The equivalent nominal stress is normalized by the initial modulus of substrate material E_0 as

$$\bar{\sigma} = \frac{P}{(2\sin\alpha_1 + \sin\alpha_2)E_0 l} \tag{1}$$

where α_i is the rotation angle between the local coordinate system and the global coordinate system ($i = 1$ or 2 denotes beam AB and BC, respectively). The incompressible Mooney–Rivlin constitutive relation [34,39] gives the uniaxial stress–strain relationship $\sigma = E_0 f(\varepsilon)$, where $f(\varepsilon)$ is

$$f(\varepsilon) = \frac{1}{15}\left(4 + \frac{1}{1+\varepsilon}\right)\left[1 + \varepsilon - \frac{1}{(1+\varepsilon)^2}\right] \tag{2}$$

The equilibrium equations of the beams in Fig. 2 give

$$\frac{\mathrm{d}Q_i}{\mathrm{d}s_i} - N_i\frac{\mathrm{d}\varphi_i}{\mathrm{d}s_i} = 0 \tag{3a}$$

$$\frac{\mathrm{d}N_i}{\mathrm{d}s_i} + Q_i\frac{\mathrm{d}\varphi_i}{\mathrm{d}s_i} = 0 \tag{3b}$$

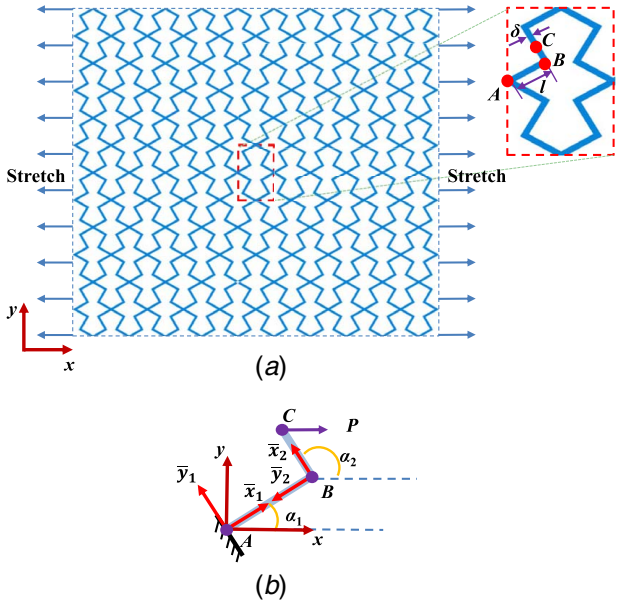

Fig. 1 Geometry of a zigzag cellular substrate: (*a*) a representative zigzag cellular substrate under uniaxial stretching, with the basic unit shown in a magnified view and (*b*) 1/8 of the basic unit.

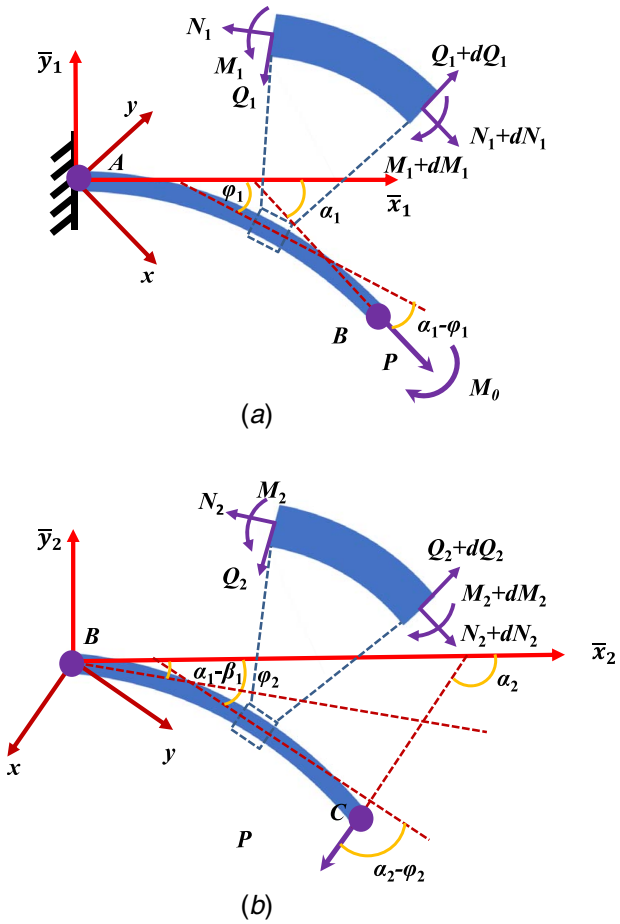

Fig. 2 Schematic illustration of the analytical model for (*a*) beam *AB* and (*b*) beam *BC*

where Q_i is the shear force, N_i is the axial force, and φ_i is the angle between the beam axial direction and $\bar{x}_i$-direction. Let S and s represent the axial length of the beam segment in zigzag cellular substrate before and after stretching, respectively. The relationship between $\mathrm{d}s_i$ and $\mathrm{d}S_i$ is

$$\frac{\mathrm{d}s_i}{\mathrm{d}S_i} = 1 + f^{-1}\left(\frac{N_i}{E_0\delta}\right) \tag{4}$$

The moment balance of the beam gives

$$\frac{\mathrm{d}M_i}{\mathrm{d}s_i} = Q_i, \text{ or } \frac{\mathrm{d}M_i}{\mathrm{d}S_i} = \left[1 + f^{-1}\left(\frac{N_i}{E_0\delta}\right)\right]Q_i \tag{5}$$

where M_i is the moment. The axial force N_i and shear force Q_i are related to P and φ_i as

$$N_i = P\cos(\alpha_i - \varphi_i) \tag{6a}$$

$$Q_i = -P\sin(\alpha_i - \varphi_i) \tag{6b}$$

The moment–curvature relation gives

$$M_i = E_0 I \mathrm{d}\varphi_i/\mathrm{d}S_i \tag{7}$$

where E_0I is the in-plane bending stiffness.

Substitution of Eqs. (6) and (7) into the moment equilibrium Eq. (5) gives

$$\frac{\mathrm{d}^2\varphi_i}{\mathrm{d}S_i^2} = -\frac{P}{E_0 I}\sin(\alpha_i - \varphi_i)\left\{1 + f^{-1}\left[\frac{P\cos(\alpha_i - \varphi_i)}{E_0\delta}\right]\right\} \tag{8}$$

For beam AB, the moment at point B is denoted by M_0, and the moment condition at point B is

$$(\mathrm{d}\varphi_1/\mathrm{d}S_1)|_{S_1=l} = \frac{M_0}{E_0 I} \tag{9}$$

Substitution of Eq. (9) into Eq. (8) gives

$$\left(\frac{\mathrm{d}\varphi_1}{\mathrm{d}S_1}\right)^2 = -\frac{2P}{E_0 I}\int_{\alpha_1-\beta_1}^{\varphi_1}\sin(\alpha_1 - x)\left\{1 + f^{-1}\left[\frac{P\cos(\alpha_1 - x)}{E_0\delta}\right]\right\}\mathrm{d}x + \left(\frac{M_0}{E_0 I}\right)^2 \tag{10}$$

where $\beta_1 = \alpha_1 - \varphi_1|_{S_1=l}$ is determined from the following equation by integrating Eq. (10) from $S_1 = 0$ to $S_1 = l$

$$l = \int_0^{\alpha_1-\beta_1} \frac{\mathrm{d}\varphi_1}{\sqrt{-\frac{2P}{E_0 I}\int_{\alpha_1-\beta_1}^{\varphi_1}\sin(\alpha_1 - x)\left\{1 + f^{-1}\left[\frac{P\cos(\alpha_1 - x)}{E_0\delta}\right]\right\}\mathrm{d}x + \left(\frac{M_0}{E_0 I}\right)^2}} \tag{11}$$

For beam BC, the moment condition at point C is

$$(\mathrm{d}\varphi_2/\mathrm{d}S_2)|_{S_2=l/2} = 0 \tag{12}$$

Substitution of Eq. (12) into Eq. (8) gives

$$\left(\frac{\mathrm{d}\varphi_2}{\mathrm{d}S_2}\right)^2 = -\frac{2P}{E_0 I}\int_{\alpha_2-\beta_2}^{\varphi_2}\sin(\alpha_2 - x)\left\{1 + f^{-1}\left[\frac{P\cos(\alpha_2 - x)}{E_0\delta}\right]\right\}\mathrm{d}x \tag{13}$$

where $\beta_2 = \alpha_2 - \varphi_2|_{S_2=l/2}$ is determined from the following equation by integrating Eq. (13) from $S_2 = 0$ to $S_2 = l/2$

$$\frac{l}{2} = \int_{\alpha_1-\beta_1}^{\alpha_2-\beta_2} \frac{\mathrm{d}\varphi_2}{\sqrt{-\frac{2P}{E_0 I}\int_{\alpha_2-\beta_2}^{\varphi_2}\sin(\alpha_2 - x)\left\{1 + f^{-1}\left[\frac{P\cos(\alpha_2 - x)}{E_0\delta}\right]\right\}\mathrm{d}x}} \tag{14}$$

where the lower limit of integration is the rotation angle, at point B, of $\alpha_1 - \beta_1$ as shown in Fig. 2(*b*). The local coordinates of points B and C can be obtained from $\mathrm{d}\bar{x}/ds_i = \cos\varphi_i$ and $\mathrm{d}\bar{y}/ds_i = \sin\varphi_i$, as

$$\begin{Bmatrix}\bar{x}_B\\ \bar{y}_B\end{Bmatrix} = \int_0^{\alpha_1-\beta_1} \frac{\left\{1 + f^{-1}\left[\frac{P\cos(\alpha_1 - \varphi_1)}{E_0\delta}\right]\right\}\begin{Bmatrix}\cos\varphi_1\\ \sin\varphi_1\end{Bmatrix}\mathrm{d}\varphi_1}{\sqrt{-\frac{2P}{E_0 I}\int_{\alpha_1-\beta_1}^{\varphi_1}\sin(\alpha_1 - x)\left\{1 + f^{-1}\left[\frac{P\cos(\alpha_1 - x)}{E_0\delta}\right]\right\}\mathrm{d}x + \left(\frac{M_0}{E_0 I}\right)^2}} \tag{15a}$$

$$\begin{Bmatrix}\bar{x}_C\\ \bar{y}_C\end{Bmatrix} = \int_{\alpha_1-\beta_1}^{\alpha_2-\beta_2} \frac{\left\{1 + f^{-1}\left[\frac{P\cos(\alpha_2 - \varphi_2)}{E_0\delta}\right]\right\}\begin{Bmatrix}\cos\varphi_2\\ \sin\varphi_2\end{Bmatrix}\mathrm{d}\varphi_2}{\sqrt{-\frac{2P}{E_0 I}\int_{\alpha_2-\beta_2}^{\varphi_2}\sin(\alpha_2 - x)\left\{1 + f^{-1}\left[\frac{P\cos(\alpha_2 - x)}{E_0\delta}\right]\right\}\mathrm{d}x}} \tag{15b}$$

where $\bar{x}$, $\bar{y}$ represent the local coordinates. The global coordinates of points B and C after deformation are related to their local coordinates by

$$\begin{cases} x_C - x_B = \bar{x}_C \cos\alpha_2 - \bar{y}_C \sin\alpha_2 \\ y_C - y_B = \bar{x}_C \sin\alpha_2 + \bar{y}_C \cos\alpha_2 \end{cases} \tag{16a}$$

$$\begin{cases} x_B = \hat{\bar{x}}_B \cos\alpha_1 - \hat{\bar{y}}_B \sin\alpha_1 \\ y_B = \hat{\bar{x}}_B \sin\alpha_1 + \hat{\bar{y}}_B \cos\alpha_1 \end{cases} \tag{16b}$$

The moment at point B can be obtained based on the global coordinates of points B and C as

$$M_0 = (y_C - y_B)P \tag{17}$$

Based on Eqs. (11), (14), (15), (16), and (17), the global coordinates of points B and C can be obtained. The global coordinates of point C before deformation are

$$X_C = \left(\cos\alpha_1 + \frac{1}{2}\cos\alpha_2\right)l \tag{18a}$$

$$Y_C = \left(\sin\alpha_1 + \frac{1}{2}\sin\alpha_2\right)l \tag{18b}$$

The nominal strain can be obtained as

$$\varepsilon_{x\_\text{celluar}} = \frac{x_C}{X_C} - 1 = \frac{\bar{x}_C\cos\alpha_2 - \bar{y}_C\sin\alpha_2 + \bar{x}_B\cos\alpha_1 - \bar{y}_B\sin\alpha_1}{\left(\cos\alpha_1 + \frac{1}{2}\cos\alpha_2\right)l} - 1 \tag{19a}$$

$$\varepsilon_{y\_\text{celluar}} = \frac{y_C}{Y_C} - 1 = \frac{\bar{x}_C\sin\alpha_2 + \bar{y}_C\cos\alpha_2 + \bar{x}_B\sin\alpha_1 + \bar{y}_B\cos\alpha_1}{\left(\sin\alpha_1 + \frac{1}{2}\sin\alpha_2\right)l} - 1 \tag{19b}$$

Based on the increments in $\varepsilon_{x\_\text{celluar}}$ and $\varepsilon_{y\_\text{celluar}}$, the equivalent Poisson's ratio is obtained as

$$\nu_{\text{celluar}} = -\frac{\mathrm{d}\varepsilon_{y\_\text{celluar}}}{\mathrm{d}\varepsilon_{x\_\text{celluar}}} \tag{20}$$

The above process can also be used to calculate the deformed shape. Similar to Eq. 15(*a*), for a specific location along beam AB with angle β_3 (the angle between x-direction and the beam axial direction along beam AB after deformation) ranging between β_1 and α_1, the local coordinates can be obtained as

$$\begin{Bmatrix} \bar{x}_{\beta_3} \\ \bar{y}_{\beta_3} \end{Bmatrix} = \int_0^{\alpha_1-\beta_3} \frac{\left\{1 + f^{-1}\left[\frac{P\cos(\alpha_1-\varphi_1)}{E_0\delta}\right]\right\}\begin{Bmatrix}\cos\varphi_1 \\ \sin\varphi_1\end{Bmatrix}\mathrm{d}\varphi_1}{\sqrt{-\frac{2P}{E_0 I}\int_{\alpha_1-\beta_1}^{\varphi_1}\sin(\alpha_1-x)\left\{1+f^{-1}\left[\frac{P\cos(\alpha_1-x)}{E_0\delta}\right]\right\}\mathrm{d}x + \left(\frac{M_0}{E_0 I}\right)^2}} \tag{21}$$

The global coordinates after deformation can be obtained based on Eq. 16(*b*)

$$\begin{cases} x_{\beta_3} = \bar{x}_{\beta_3}\cos\alpha_1 - \bar{y}_{\beta_3}\sin\alpha_1 \\ y_{\beta_3} = \bar{x}_{\beta_3}\sin\alpha_1 + \bar{y}_{\beta_3}\cos\alpha_1 \end{cases} \tag{22}$$

Similar to Eq. 15(*b*), for a specific location along beam BC with angle β_4 (the angle between x-direction and the beam axial direction along beam BC after deformation) ranging between β_2 and $\alpha_2 - \alpha_1 + \beta_1$, the local coordinates can be obtained as

$$\begin{Bmatrix} \bar{x}_{\beta_4} \\ \bar{y}_{\beta_4} \end{Bmatrix} = \int_{\alpha_1-\beta_1}^{\alpha_2-\beta_4} \frac{\left\{1 + f^{-1}\left[\frac{P\cos(\alpha_2-\varphi_2)}{E_0\delta}\right]\right\}\begin{Bmatrix}\cos\varphi_2 \\ \sin\varphi_2\end{Bmatrix}\mathrm{d}\varphi_2}{\sqrt{-\frac{2P}{E_0 I}\int_{\alpha_2-\beta_2}^{\varphi_2}\sin(\alpha_2-x)\left\{1+f^{-1}\left[\frac{P\cos(\alpha_2-x)}{E_0\delta}\right]\right\}\mathrm{d}x}} \tag{23}$$

The global coordinates after deformation can be obtained based on Eq. 16(*a*)

$$\begin{cases} x_{\beta_4} = \bar{x}_B\cos\alpha_1 - \bar{y}_B\sin\alpha_1 + \bar{x}_{\beta_4}\cos\alpha_2 - \bar{y}_{\beta_4}\sin\alpha_2 \\ y_{\beta_4} = \bar{x}_B\sin\alpha_1 + \bar{y}_B\cos\alpha_1 + \bar{x}_{\beta_4}\sin\alpha_2 + \bar{y}_{\beta_4}\cos\alpha_2 \end{cases} \tag{24}$$

3 Results

Figure 3 compares the deformed shape predicted by the proposed analytical model and that by FEA, with $\alpha_1 = 30$ deg, $\alpha_2 = 120$ deg, $\delta = 0.1\,l$, and $l = 0.3$ mm at different stretching strains. Four-node shell elements are chosen for the cellular substrate in the commercial FEA software suite ABAQUS. The deformed shape calculated by the analytical model agrees well with that extracted directly from FEA.

The stress–strain curves predicted by FEA and the analytical model for the zigzag cellular substrates are demonstrated in Fig. 4. Figure 4(*a*) manifests the stress–strain curves with $\alpha_1 = 30$ deg, $\alpha_2 = 120$ deg for different widths. Figure 4(*b*) shows the stress–strain curves with $\delta = 0.1\,l$, $\alpha_2 - \alpha_1 = 90$ deg for different angles α_1. Figure 4(*c*) illustrates the stress–strain curves with $\delta = 0.1\,l$, $\alpha_1 = 30$ deg for different angle differences α_2–α_1. The results of parameter analysis show that a lower equivalent modulus can be obtained with a smaller width and a slenderer (larger lateral-parallel aspect ratio when uniaxially stretched; described by larger α_1) and wavier (longer curve length within the same span; described by larger (α_2–α_1)) zigzag shape. The stress–strain responses calculated by the analytical model agree well with the FEA results.

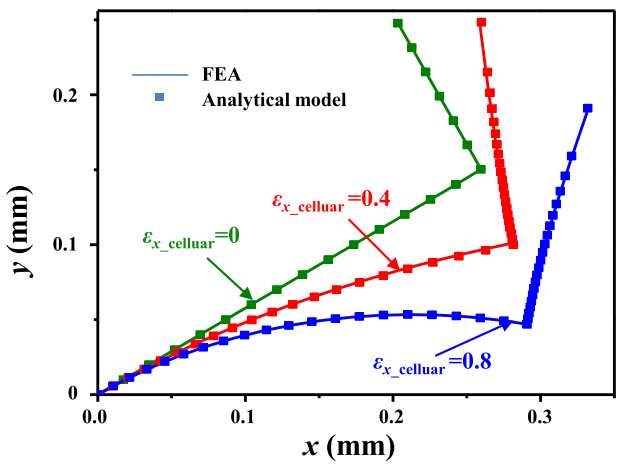

Fig. 3 Comparison of the deformed shapes of zigzag cellular substrate predicted by the analytical model and FEA under different stretching strains

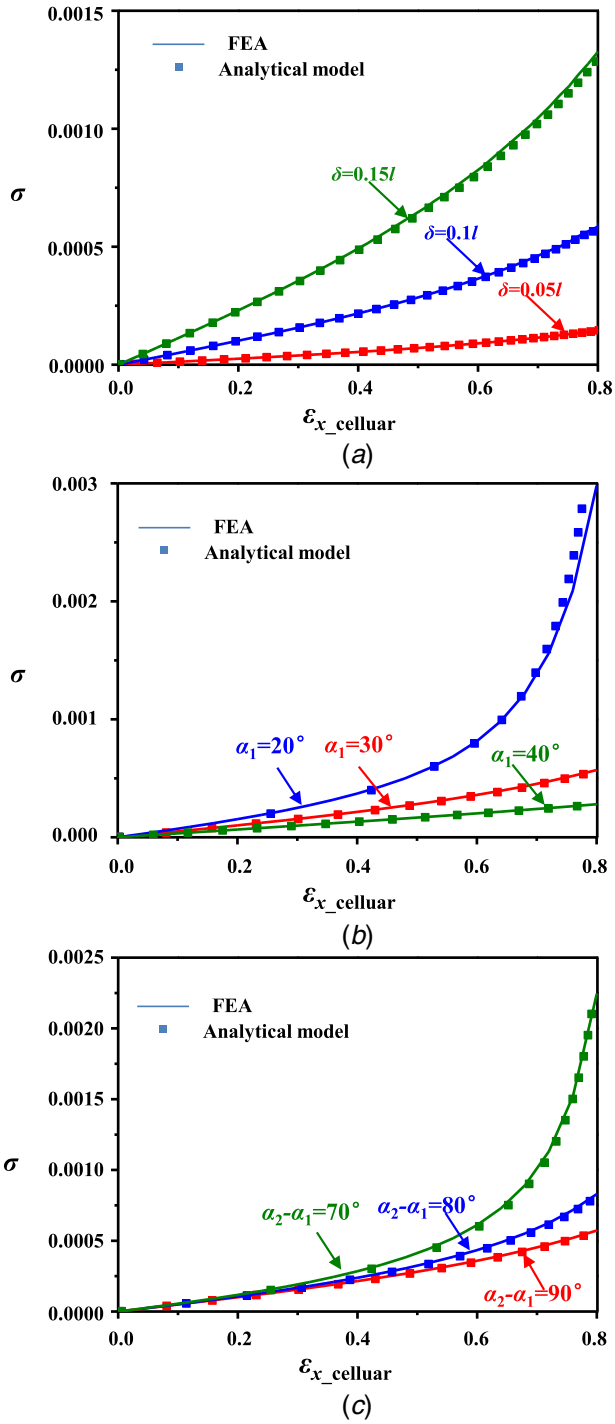

Fig. 4 Relationship between the normalized nominal stress (σ) and the stretching strain ($\varepsilon_{x\_celluar}$) for (*a*) different width, (*b*) different α_1 ($\alpha_2-\alpha_1 = 90$ deg), and (*c*) different $\alpha_2-\alpha_1$

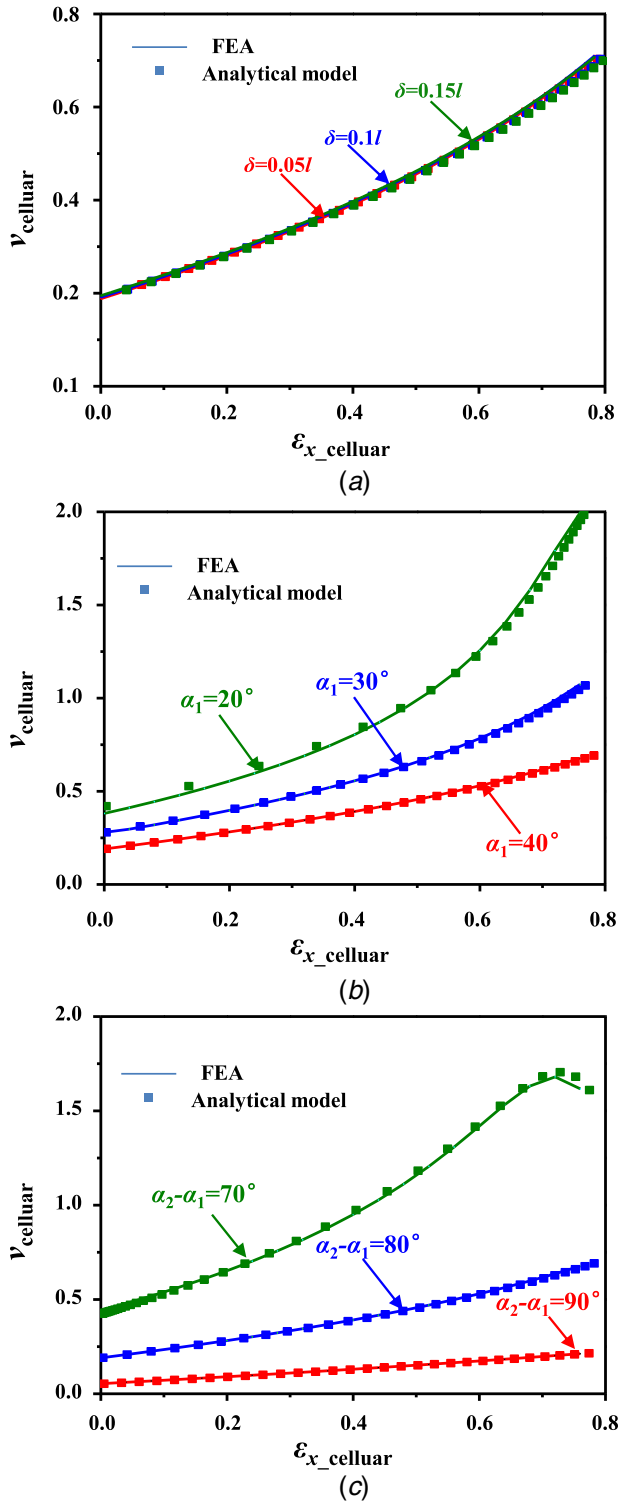

Fig. 5 Relationship between the Poisson's ratio ($\nu_{celluar}$) and the stretching strain ($\varepsilon_{x\_celluar}$) for (*a*) different width, (*b*) different α_1 ($\alpha_2-\alpha_1 = 90$ deg), and (*c*) different $\alpha_2-\alpha_1$

Figure 5 presents the Poisson's ratio–strain curves calculated by the analytical model and predicted by FEA for the zigzag cellular substrates. Poisson's ratio versus stretching strain with $\alpha_1 = 30$ deg, $\alpha_2 = 120$ deg for different widths is shown in Fig. 5(*a*). The width has a noticeable effect on the Poisson's ratio. Figure 5(*b*) illustrates Poisson's ratio versus stretching strain with $\delta = 0.1\,l$, $\alpha_2-\alpha_1 = 90$ deg for different angles α_1. The response of Poisson's ratio versus stretching strain with $\delta = 0.1\,l$, $\alpha_1 = 30$ deg for different angle differences $\alpha_2-\alpha_1$ is presented in Fig. 5(*c*). Results show that a slenderer (described by larger α_1) and wavier (described by larger $(\alpha_2-\alpha_1)$) zigzag shape yields a lower Poisson's ratio. The Poisson's ratio–strain relations calculated by the analytical model perfectly match the FEA results.

The zigzag cellular substrates possess an advantageous feature over the previously reported hexagonal cellular substrates in terms of reducing their restriction on the natural motion of human skin, by inducing a lower interfacial shear stress between the substrate and skin. Figures 6(*a*) and 6(*b*) manifests two representative cellular geometries (thickness 0.3 mm, porosity 80%, dimensions

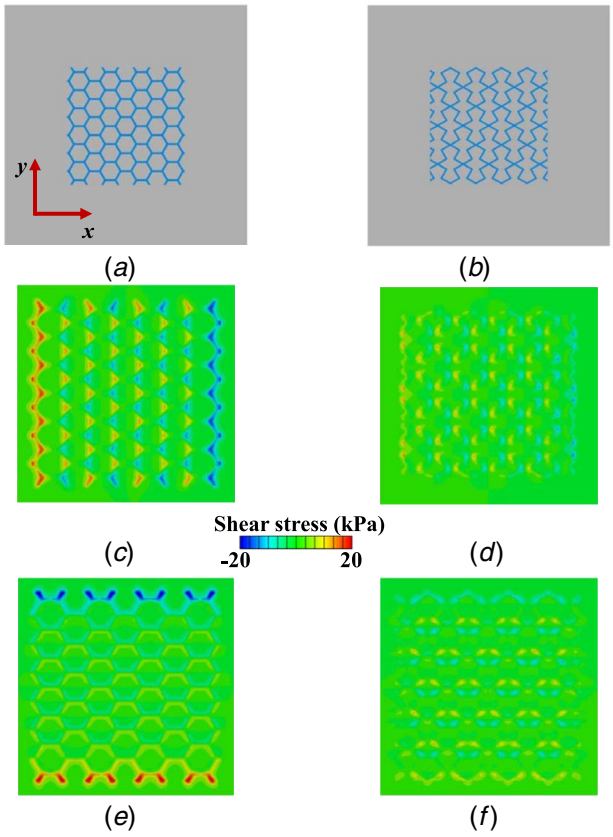

Fig. 6 Interfacial shear stress distribution (on the skin) between the cellular substrate and the skin. Schematic illustrations of hexagonal (*a*) and zigzag (*b*) cellular substrates bonded to the skin. The shear stress contours when (*c*) stretching a hexagonal cellular substrate along *x*-direction, (*d*) stretching a zigzag cellular substrate along *x*-direction, (*e*) stretching a hexagonal cellular substrate along *y*-direction, or (*f*) stretching a zigzag cellular substrate along *y*-direction.

3.4 mm × 3.4 mm, elastic modulus of elastomer substrate material 500 kPa) bonded to the skin (thickness 1 mm, elastic modulus 130 kPa [41]). The porosity ψ of the zigzag cellular substrate is calculated as [35,40]

$$\psi = 1 - \frac{3\delta}{(2\cos\alpha_1 + \cos\alpha_2)(2\sin\alpha_1 + \sin\alpha_2)l} \tag{25}$$

The shear stress between the cellular substrates and the skin is computed using FEA where the cellular substrates are modeled with four-node shell elements and the skin with eight-node solid elements. Figures 6(*c*) and 6(*d*) gives the shear stress between the cellular substrate and the skin under 50% uniaxial stretching of the skin along *x*-direction. The maximum interfacial shear stress along the stretching direction between the skin and the zigzag cellular substrate (Fig. 6(*d*)) is 14.8 kPa, which is smaller than the human skin sensitivity of 20 kPa [38], suggesting smaller constraints on the skin than the hexagonal cellular substrate (Fig. 6(*c*)). The same phenomenon also holds when stretching along *y*-direction, as shown in Figs. 6(*e*) and 6(*f*). The interfacial shear stress distribution is insensitive to a moderate increase of cellular substrate thickness.

Figure 7 shows the dependence of the interfacial shear stress (on the skin) on the stretching direction (which is denoted by the angle between the stretching direction and the positive *x*-direction (in Fig. 6)), for hexagonal and zigzag cellular substrates. S_{13} and S_{23} are the interfacial shear stress components along and perpendicular to the stretching direction, respectively. Whatever the stretching

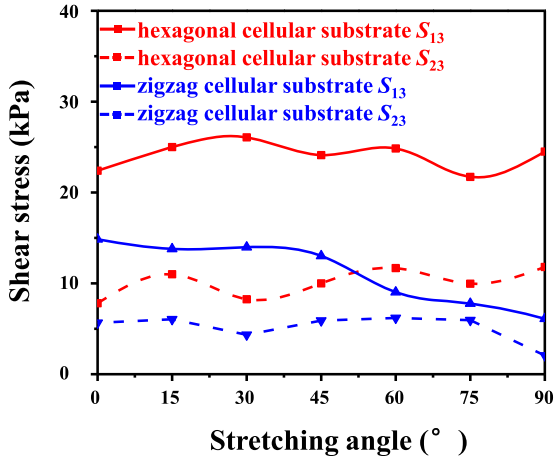

Fig. 7 Comparison of the interfacial shear stress (on the skin) induced by the zigzag and hexagonal cellular substrates along different stretching directions (described by different stretching angles)

direction, both S_{13} and S_{23} with the zigzag cellular substrate are lower than those with the hexagonal cellular substrate. The maximum shear stress between the zigzag cellular substrate and the skin is noticeably lower than the human skin sensitivity of 20 kPa for any stretching direction. Lower constraints on the natural movement of skin could be achieved using the zigzag cellular substrates.

4 Conclusions

An analytical model of zigzag cellular substrates under finite deformation is proposed. The deformed shape, nonlinear stress–strain curves and Poisson's ratio–strain curves can be conveniently calculated by the reported analytical model and agree well with FEA predictions. The results of parameter analysis show that a smaller width and a slenderer (larger aspect ratio) and wavier (longer curve length within the same span) zigzag shape yield a lower equivalent modulus and a lower Poisson's ratio for the zigzag cellular substrates. Whatever the stretching direction of skin, the skin-mounted zigzag cellular substrates could achieve lower constraints on the natural motion of human skin compared with those hexagonal cellular substrates, suggesting promising application opportunities toward mechanically "invisible" epidermal electronics.

Acknowledgment

The authors gratefully acknowledge the support from the National Natural Science Foundation of China under Grant Nos. 11972059 and 11572023. Y. H. acknowledges the support from the National Science Foundation, USA (Grant No. CMMI1635443).

References

[1] Kim, H.-J., Thukral, A., and Yu, C., 2018, "Highly Sensitive and Very Stretchable Strain Sensor Based on a Rubbery Semiconductor," ACS Appl. Mater. Interfaces, **10**(5), pp. 5000–5006.
[2] Tao, L.-Q., Tian, H., Liu, Y., Ju, Z.-Y., Pang, Y., Chen, Y.-Q., Wang, D.-Y., Tian, X.-G., Yan, J.-C., Deng, N.-Q., Yang, Y., and Ren, T.-L., 2017, "An Intelligent Artificial Throat With Sound-Sensing Ability Based on Laser Induced Graphene," Nat. Commun., **8**, p. 14579.
[3] Kim, Y., Chortos, A., Xu, W., Liu, Y., Oh, J. Y., Son, D., Kang, J., Foudeh, A. M., Zhu, C., Lee, Y., Niu, S., Liu, J., Pfattner, R., Bao, Z., and Lee, T.-W., 2018, "A Bioinspired Flexible Organic Artificial Afferent Nerve," Science, **360**(6392), pp. 998–1003.

[4] Khang, D.-Y., Jiang, H., Huang, Y., and Rogers, J. A., 2006, "A Stretchable Form of Single-Crystal Silicon for High-Performance Electronics on Rubber Substrates," Science, **311**(5758), pp. 208–212.
[5] Avila, R., and Xue, Y., 2017, "Torsional Buckling by Joining Prestrained and Unstrained Elastomeric Strips With Application as Bilinear Elastic Spring," ASME J. Appl. Mech., **84**(10), p. 104502.
[6] Zhang, P., and Parnell, W. J., 2017, "Band Gap Formation and Tunability in Stretchable Serpentine Interconnects," ASME J. Appl. Mech., **84**(9), p. 091007.
[7] Li, Y., Zhang, J., Xing, Y., and Song, J., 2017, "Thermomechanical Analysis of Epidermal Electronic Devices Integrated With Human Skin," ASME J. Appl. Mech., **84**(11), p. 111004.
[8] Wang, A., Avila, R., and Ma, Y., 2017, "Mechanics Design for Buckling of Thin Ribbons on an Elastomeric Substrate Without Material Failure," ASME J. Appl. Mech., **84**(9), p. 094501.
[9] Zhang, M., Liu, H., Cao, P., Chen, B., Hu, J., Chen, Y., Pan, B., Fan, J. A., Li, R., Zhang, L., and Su, Y., 2017, "Strain-Limiting Substrates Based on Nonbuckling, Prestrain-Free Mechanics for Robust Stretchable Electronics," ASME J. Appl. Mech., **84**(12), p. 121010.
[10] Xu, Z., Fan, Z., Zi, Y., Zhang, Y., and Huang, Y., 2019, "An Inverse Design Method of Buckling-Guided Assembly for Ribbon-Type 3D Structures," ASME J. Appl. Mech., **87**(3), p. 031004.
[11] Ma, Y., Choi, J., Hourlier-Fargette, A., Xue, Y., Chung, H. U., Lee, J. Y., Wang, X., Xie, Z., Kang, D., Wang, H., Han, S., Kang, S.-K., Kang, Y., Yu, X., Slepian, M. J., Raj, M. S., Model, J. B., Feng, X., Ghaffari, R., Rogers, J. A., and Huang, Y., 2018, "Relation Between Blood Pressure and Pulse Wave Velocity for Human Arteries," Proc. Natl. Acad. Sci. U. S. A., **115**(44), pp. 11144–11149.
[12] Yang, S., Qiao, S., and Lu, N., 2016, "Elasticity Solutions to Nonbuckling Serpentine Ribbons," ASME J. Appl. Mech., **84**(2), p. 021004.
[13] Yan, Z., Wang, B., and Wang, K., 2019, "Stretchability and Compressibility of a Novel Layout Design for Flexible Electronics Based on Bended Wrinkle Geometries," Composites, Part B, **166**, pp. 65–73.
[14] Yan, Z., Wang, B., Wang, K., and Zhang, C., 2019, "A Novel Cellular Substrate for Flexible Electronics With Negative Poisson Ratios Under Large Stretching," Int. J. Mech. Sci., **151**, pp. 314–321.
[15] Zhang, Y., Jiao, Y., Wu, J., Ma, Y., and Feng, X., 2020, "Configurations Evolution of a Buckled Ribbon in Response to Out-of-Plane Loading," Extreme Mech. Lett., **34**, p. 100604.
[16] Yan, Z., Wang, B., Wang, K., Zhao, S., Li, S., Huang, Y., and Wang, H., 2019, "Cellular Substrate to Facilitate Global Buckling of Serpentine Structures," ASME J. Appl. Mech., **87**(2), p. 024501.
[17] Yu, X., Xie, Z., Yu, Y., Lee, J., Vazquez-Guardado, A., Luan, H., Ruban, J., Ning, X., Akhtar, A., Li, D., Ji, B., Liu, Y., Sun, R., Cao, J., Huo, Q., Zhong, Y., Lee, C. M., Kim, S. Y., Gutruf, P., Zhang, C., Xue, Y., Guo, Q., Chempakasseril, A., Tian, P., Lu, W., Jeong, J. Y., Yu, Y. J., Cornman, J., Tan, C. S., Kim, B. H., Lee, K. H., Feng, X., Huang, Y., and Rogers, J. A., 2019, "Skin-Integrated Wireless Haptic Interfaces for Virtual and Augmented Reality," Nature, **575**(7783), pp. 473–479.
[18] Li, J., Zhao, J., and Rogers, J. A., 2019, "Materials and Designs for Power Supply Systems in Skin-Interfaced Electronics," Acc. Chem. Res., **52**(1), pp. 53–62.
[19] Kim, N., Lim, T., Song, K., Yang, S., and Lee, J., 2016, "Stretchable Multichannel Electromyography Sensor Array Covering Large Area for Controlling Home Electronics With Distinguishable Signals From Multiple Muscles," ACS Appl. Mater. Interaces, **8**(32), pp. 21070–21076.
[20] Yang, W., Sherman, V. R., Gludovatz, B., Schaible, E., Stewart, P., Ritchie, R. O., and Meyers, M. A., 2015, "On the Tear Resistance of Skin," Nat. Commun., **6**, p. 6649.
[21] Ling, S., Zhang, Q., Kaplan, D. L., Omenetto, F., Buehler, M. J., and Qin, Z., 2016, "Printing of Stretchable Silk Membranes for Strain Measurements," Lab Chip, **16**(13), pp. 2459–2466.
[22] Meyers, M. A., McKittrick, J., and Chen, P. Y., 2013, "Structural Biological Materials: Critical Mechanics-Materials Connections," Science, **339**(6121), pp. 773–779.
[23] Cranford, S. W., Tarakanova, A., Pugno, N. M., and Buehler, M. J., 2012, "Nonlinear Material Behaviour of Spider Silk Yields Robust Webs," Nature, **482**(7383), pp. 72–76.
[24] Ma, Q., Cheng, H., Jang, K. I., Luan, H., Hwang, K. C., Rogers, J. A., Huang, Y., and Zhang, Y., 2016, "A Nonlinear Mechanics Model of Bio-Inspired Hierarchical Lattice Materials Consisting of Horseshoe Microstructures," J. Mech. Phys. Solids, **90**, pp. 179–202.
[25] Lee, Y. K., Jang, K.-I., Ma, Y., Koh, A., Chen, H., Jung, H. N., Kim, Y., Kwak, J. W., Wang, L., Xue, Y., Yang, Y., Tian, W., Jiang, Y., Zhang, Y., Feng, X., Huang, Y., and Rogers, J. A., 2017, "Chemical Sensing Systems That Utilize Soft Electronics on Thin Elastomeric Substrates With Open Cellular Designs," Adv. Funct. Mater., **27**(9), p. 1605476.
[26] Ma, Y., Feng, X., Rogers, J. A., Huang, Y., and Zhang, Y., 2017, "Design and Application of 'J-Shaped' Stress–Strain Behavior in Stretchable Electronics: A Review," Lab Chip, **17**(10), pp. 1689–1704.
[27] Lee, C. H., Ma, Y., Jang, K.-I., Banks, A., Pan, T., Feng, X., Kim, J. S., Kang, D., Raj, M. S., McGrane, B. L., Morey, B., Wang, X., Ghaffari, R., Huang, Y., and Rogers, J. A., 2015, "Soft Core/Shell Packages for Stretchable Electronics," Adv. Funct. Mater., **25**(24), pp. 3698–3704.
[28] Liu, J., and Zhang, Y., 2018, "A Mechanics Model of Soft Network Materials With Periodic Lattices of Arbitrarily Shaped Filamentary Microstructures for Tunable Poisson's Ratios," ASME J. Appl. Mech., **85**(5), p. 051003.
[29] Zhang, E., Liu, Y., and Zhang, Y., 2018, "A Computational Model of Bio-Inspired Soft Network Materials for Analyzing Their Anisotropic Mechanical Properties," ASME J. Appl. Mech., **85**(7), p. 071002.
[30] Liu, J., and Zhang, Y., 2018, "Soft Network Materials With Isotropic Negative Poisson's Ratios Over Large Strains," Soft Matter, **14**(5), pp. 693–703.
[31] Ma, Y., Zhang, Y., Cai, S., Han, Z., Liu, X., Wang, F., Cao, Y., Wang, Z., Li, H., Chen, Y., and Feng, X., 2019, "Flexible Hybrid Electronics for Digital Healthcare," Adv. Mater., p. 1902062.
[32] Dou, Y., Jin, M., Zhou, G., and Shui, L., 2015, "Breath Figure Method for Construction of Honeycomb Films," Membranes, **5**(3), pp. 399–424.
[33] Jang, K.-I., Chung, H. U., Xu, S., Lee, C. H., Luan, H., Jeong, J., Cheng, H., Kim, G.-T., Han, S. Y., Lee, J. W., Kim, J., Cho, M., Miao, F., Yang, Y., Jung, H. N., Flavin, M., Liu, H., Kong, G. W., Yu, K. J., Rhee, S. I., Chung, J., Kim, B., Kwak, J. W., Yun, M. H., Kim, J. Y., Song, Y. M., Paik, U., Zhang, Y., Huang, Y., and Rogers, J. A., 2015, "Soft Network Composite Materials With Deterministic and Bio-Inspired Designs," Nat. Commun., **6**, p. 6566.
[34] Chen, H., Zhu, F., Jang, K.-I., Feng, X., Rogers, J. A., Zhang, Y., Huang, Y., and Ma, Y., 2018, "The Equivalent Medium of Cellular Substrate Under Large Stretching, With Applications to Stretchable Electronics," J. Mech. Phys. Solids, **120**, pp. 199–207.
[35] Zhu, F., Xiao, H., Li, H., Huang, Y., and Ma, Y., 2019, "Irregular Hexagonal Cellular Substrate for Stretchable Electronics," ASME J. Appl. Mech., **86**(3), p. 034501.
[36] Tancogne-Dejean, T., Karathanasopoulos, N., and Mohr, D., 2019, "Stiffness and Strength of Hexachiral Honeycomb-Like Metamaterials," ASME J. Appl. Mech., **86**(11), p. 111010.
[37] Zhu, F., Xiao, H., Xue, Y., Feng, X., Huang, Y., and Ma, Y., 2018, "Anisotropic Mechanics of Cellular Substrate Under Finite Deformation," ASME J. Appl. Mech., **85**(7), p. 071007.
[38] Wang, S., Li, M., Wu, J., Kim, D.-H., Lu, N., Su, Y., Kang, Z., Huang, Y., and Rogers, J. A., 2012, "Mechanics of Epidermal Electronics," ASME J. Appl. Mech., **79**(3), p. 031022.
[39] Mooney, M., 1940, "A Theory of Large Elastic Deformation," J. Appl. Phys., **11**(9), pp. 582–592.
[40] Gibson, L. J., and Ashby, M. F., 1999, *Cellular Solids: Structure and Properties*, Cambridge University Press, Cambridge, UK.
[41] Schwindt, D. A., Wilhelm, K.-P., Miller, D. L., and Maibach, H. I., 1998, "Cumulative Irritation in Older and Younger Skin: A Comparison," Acta. Derm.-Venereol., **78**(4), pp. 279–283.